

RSC Advances



This is an *Accepted Manuscript*, which has been through the Royal Society of Chemistry peer review process and has been accepted for publication.

Accepted Manuscripts are published online shortly after acceptance, before technical editing, formatting and proof reading. Using this free service, authors can make their results available to the community, in citable form, before we publish the edited article. This *Accepted Manuscript* will be replaced by the edited, formatted and paginated article as soon as this is available.

You can find more information about *Accepted Manuscripts* in the [Information for Authors](#).

Please note that technical editing may introduce minor changes to the text and/or graphics, which may alter content. The journal's standard [Terms & Conditions](#) and the [Ethical guidelines](#) still apply. In no event shall the Royal Society of Chemistry be held responsible for any errors or omissions in this *Accepted Manuscript* or any consequences arising from the use of any information it contains.

Anticorrosive Oligoaniline-Contained Electroactive Siliceous Hybrid Materials

Lin Gu¹, Shuan Liu^{1*}, Haichao Zhao^{1*}, Haibin Yu¹

¹Key Laboratory of Marine Materials and Related Technologies, Zhejiang Key
Laboratory of Marine Materials and Protective Technologies, Ningbo Institute of
Materials Technology and Engineering, Chinese Academy of Sciences, Ningbo
315201, P. R. China

* Corresponding author: Tel.: +86 0574 87911126.

E-mail addresses: liushuan@nimte.ac.cn; zhaohaichao@nimte.ac.cn

Abstract

In this work, a novel electroactive silsesquioxane precursor, *N*-(3-triethoxysilylpropylureido) aniline tetramer (TESPAT) was synthesized via one-step coupling reaction between phenyl-capped aniline tetramer (AT) and 3-(triethoxysilyl)propyl isocyanate (TESPIC) in a mild condition. The chemical structure and electroactivity of the resulting silsesquioxane precursor were investigated by FTIR, NMR, UV-vis spectra, and cyclic voltammetry. Subsequently, the sol-gel reactions of TESPAT with triethoxymethylsilane (TEMS) at various compositions were carried out to achieve new electroactive siliceous hybrid materials with good thermal stability. Furthermore, polarization curves and electrochemical impedance spectroscopic (EIS) measurements indicated that the obtained hybrid materials exhibit remarkably enhanced corrosion protection on Q235 electrodes as compared to pure silica coating. The significantly improved anticorrosion performance is attributed to the redox catalytic capabilities of the AT units in the hybrid materials.

Keywords: oligoaniline; electroactivity; corrosion; siliceous hybrid materials; silsesquioxane precursor

1. Introduction

Silica-based organic-inorganic hybrid materials have attracted a great deal of attention during the last decade since they combine the advantages of organic and inorganic components, and have found numerous applications in many fields such as optical devices,¹ chemical and biological sensors,² catalysts,³ biofouling⁴ and corrosion protection⁵. It is noteworthy that the versatility of sol-gel process enables a wide range of organically-modified silica-based hybrid materials to be made under mild conditions.⁶ Incorporating organic components into inorganic silica offers extensive possibilities to tune the structure and properties of the final materials.⁷ As far as corrosion protection is concerned, organic inhibitors have also been introduced into the sol-gel system, therefore, providing different mechanism of corrosion protection for metallic substrates without using toxic heavy metals.^{7,8} However, to the best of our knowledge, there are still few reports on the incorporation of electroactive polymers as corrosion inhibitors into inorganic silica materials for advanced anticorrosive coatings.^{9,10}

Intrinsically conducting polymers, such as polyaniline (PAN), polypyrrole, and polythiophene, have emerged as attractive materials due to their potentially commercial applications in electrode materials,^{11,12} photo-electronic devices,¹³ and sensors,¹⁴ etc. Among these electroactive polymers, PAN has been known to be one of the most promising materials in anticorrosion coatings as an alternative to chromium-containing systems because of its environmental stability, chemical redox reversibility, and relatively low cost.^{9,15-18} More interestingly, it has been reported that

PAN coatings can protect metal even at coating defect.¹⁸ However, the poor solubility of PAN in many organic solvents has limited its practical applications. Compared with PAN, oligoaniline exhibits excellent solubility and well-defined molecular structures.^{19,20} Moreover, the electroactivity of aniline oligomer is remarkably similar to that of PAN.²¹⁻²³ Therefore, aniline oligomer offers the opportunities to design and produce well-defined species with anticorrosive performance.

Our study aims to covalently incorporate electroactive organic species as corrosion inhibitors into inorganic silica for advanced anticorrosive coatings. In this paper, a novel aniline tetramer-siliceous precursor, *N*-(3-triethoxysilylpropylureido) aniline tetramer (TESPAT) was successfully synthesized for the first time via one-step coupling reaction between phenyl-capped aniline tetramer (AT) and 3-(triethoxysilyl)propyl isocyanate (TESPIC). The new aniline tetramer-siliceous compound was extensively characterized by FTIR, NMR, UV-vis spectra, and cyclic voltammetry. Subsequently, new electroactive siliceous hybrid materials have also been prepared through the sol-gel reactions of TESPAT with triethoxymethylsilane (TEMS) at various compositions. The hybrid materials exhibit remarkably enhanced corrosion protection as compared to pure silica coating, based on a series of electrochemical measurements performed under a saline condition.

2. Experimental

2.1 Materials

3-(Triethoxysilyl)propyl isocyanate (TESPIC), anhydrous tetrahydrofuran (THF), 4-amino diphenylamine and triethoxymethylsilane (TEMS) were purchased from

Aladdin Industrial Corporation, and were used without further purification. Concentrated HCl, acetone, ammonium hydroxide and petroleum ether are analytically pure, and were used as received. The Q235 steel was polished with 800 and 1,500 sand paper, and then degreased by ultrasonication in acetone.

2.2 Synthesis of Aniline Tetramer (AT)

The aniline tetramer was prepared according to the literature.²⁴ In brief, 4-amino diphenylamine (7.36 g, 40 mmol) was dissolved in a mixture of acetone (200 mL), concentrated HCl (50 mL) and water (200 mL) at 0 °C in an ice bath. Ammonium persulfate (9.13 g, 40 mmol) in acetone/water (50 mL/50 mL) solution was then added dropwise into the above solution during 1 h with vigorous stirring. The reaction was carried out in air for 4 h. The mixture was filtered to collect the AT, the cake was then washed with 200 mL of 0.1 M HCl and 100 mL of water. The AT was dedoped in 200 mL of 1 M NH₄OH for 4 h, and was filtered and washed with water until the filtrate was neutral. Finally, the AT was dried at 60 °C in vacuum for 48 h. Yield: ~95%.

2.3 Synthesis of *N*-(3-triethoxysilylpropylureido) Aniline Tetramer (TESPAT)

Aniline tetramer (3g, 8.18 mmol) was added into a three-neck round flask contained anhydrous THF (40 mL) and 3-(triethoxysilyl)propyl isocyanate (TESPIC, 2.4g, 9.7 mmol) under magnetic stirring before refluxing for 24 h under N₂ atmosphere. After the reaction was cooled down to room temperature, 200 mL of petroleum ether was added dropwise into the solution. The black solid was collected by filtration. Further purification was achieved by reprecipitation from

THF/petroleum ether, and then dried at 60 °C in vacuum till constant weight. Yield: ~98%.

2.4 Preparation of Tetramer-containing Sol-gel Solution and Coating Deposition

A convenient sol-gel approach was used to prepare novel electroactive aniline tetramer-containing hybrid materials. Typically, TEMS (1.78 g, 0.01mol) was added to a mixture of 0.01 mol/L formic acid solution (2 g) and ethanol (3.2 g) with continuous stirring for 1 h to obtain a clear solution (sol A). Meanwhile, 2 g (3.2 mmol) of TESPAT were dissolved in 98 g of ethanol. After bath-sonication for 10 min, a homogeneous solution (sol B) was formed. Sol B was then mixed with sol A at various weight ratios (referred as 2 wt%, 5 wt% and 10 wt%) according to the wt% of TESPAT in the content of TEMS. The mixed sols were kept stirring at room temperature for 24 h.

Q235 steel electrodes were immersed into the above mixed sols for 2 min at room temperature and dried at 100 °C for 1 h in an air oven.

2.5 Characterizations

¹H NMR spectra were recorded at room temperature on a NMR spectrometer (400 MHz AVANCE III, Bruker) in deuterated dimethyl sulfoxide (DMSO-*d*₆). FTIR spectra were performed on a spectrometer (NICOLET 6700, Thermo) by collecting 32 scans at a spectral resolution of 4 cm⁻¹. UV-vis spectra were obtained using a UV-vis spectrometer (Lambda 950, Perkin-Elmer). Thermo gravimetry analysis (TGA) was tested on a Perkin-Elmer Pyris Diamond thermal analyzer under a N₂ atmosphere at a heating rate of 20 °C/min from 30 °C to 500 °C.

Electrochemical impedance spectroscopy (EIS) was performed on a CHI-660E electrochemical system in 3.5 wt% NaCl aqueous solution. A classical three-electrode cell system was employed, consisting of a coating/Q235 steel as the working electrode, a saturated calomel electrode (SCE) equipped with a Luggin capillary as the reference electrode and a platinum plate of 2.5 cm² as the counter electrode. For EIS, the test frequency range was 10⁵-10⁻² Hz and the amplitude of the sinusoidal voltage signal was 20-50 mV. EIS data were analyzed by ZsimpWin 3.21 software. Polarization curves were recorded from -200 mV to +200 mV versus open circuit potential (OCP) by changing the electrode potential automatically with a scan rate of 0.5 mV/s. Cyclic voltammetry (CV) measurements were carried out in aqueous HCl solution (1 M) or anhydrous propylene carbonate (PC) containing 1 M LiClO₄. A glass carbon electrode was used as the working electrode. The scan rate was 20 mV/s.

3 Results and Discussion

3.1 Synthesis and Characterization of TESPAT

3.1.1 Synthesis and Structure Analysis of TESPAT

N-(3-triethoxysilylpropylureido) aniline tetramer (TESPAT) was synthesized based on the reaction between the amino groups of AT and the isocyanate groups of TESPIC, as shown in Scheme 1.

The obtained TESPAT was characterized by FTIR, ¹H NMR and UV-vis spectra. Figure 1 shows FTIR spectra of the AT and TESPAT. The sharp absorption peaks at 3024, 1596, and 1504 cm⁻¹ are assigned to stretching vibrations of the phenyl C-H, quinoid and benzenoid ring, respectively. The peaks at 1301 and 1221 cm⁻¹ belong to

stretching vibrations of the C-N groups. As can be seen from curve b, the new sharp absorption peaks at ca. 2900 cm^{-1} are attributed to the presence of aliphatic sp^3 C-H stretching vibrations, while sharp absorption peaks at 1641 and 1166 cm^{-1} are ascribed to stretching vibrations of C=O in the ureido unit (-NH-CO-NH-) and C-O in $-\text{OCH}_2\text{CH}_3$ group, respectively, indicating that a reaction has occurred between the amino groups of AT with the isocyanate groups of TESPIC.

Figure 2 shows ^1H NMR spectra of the AT and TESPAT. The signals assigned to the $-\text{NH}_2$ and $-\text{NH}$ groups of AT are present at 5.5 and 8.3 ppm, respectively (Figure 2a). However, the signal at 5.5 ppm has totally disappeared in Figure 2b for TESPAT, which further demonstrated the occurrence of the reaction between $-\text{NH}_2$ groups of AT and the isocyanate groups of TESPIC. The $-\text{NH}$ group signal at 8.3 ppm still exists after the reaction of TESPIC with AT, suggesting that the coupling reaction only took place at the end group of aniline tetramer (AT). Furthermore, the new peaks at 3.0, 1.5 and 0.5 ppm are assigned to the CH_2 groups between the ureido unit and siloxy group ($-\text{Si}(\text{OEt})_3$), while the signals at 3.7 and 1.1 ppm are ascribed to the CH_2 and CH_3 groups in $-\text{OCH}_2\text{CH}_3$ unit, respectively.

Figure 3 shows UV-vis spectra of the AT and TESPAT in ethanol. The pure TA shows two distinct absorption peaks at 314 and 594 nm (curve a), which are assigned to the $\pi-\pi^*$ transition of the benzene ring and the benzenoid (B) to quinoid (Q) $\pi_{\text{B}}-\pi_{\text{Q}}$ excitonic transition.²⁵⁻²⁷ Similar to AT, the TESPAT exhibit two distinct absorption peaks at 311 and 587 nm (curve b). However, the Q/B intensity ratio of TESPAT decreased along with a slight blue shift, which may be ascribed to enhanced resonance

from the formation of ureido moiety that facilitates the delocalization of electrons in benzene units.²⁸ This also confirmed that a coupling reaction had occurred between AT and TESPIC.

3.1.2 Electrochemical Characterization of TESPAT

As is well known, oligoanilines similar to polyanilines have different oxidation states (that is, leucoemeraldine base (LEB), emeraldine base (EB), and pernigraniline base (PB)) when they are treated by oxidizing and reducing agents or upon on different voltages.²⁹ The electrochemical properties of the as-prepared TESPAT were investigated by cyclic voltammetry (CV), as is shown in Figure 4. There are two pairs of well-defined oxidation peaks at 0.341 and 0.490 V, which can be assigned to the transition from a LEB form to an EB form and a further transition to a PB form, respectively (Scheme 2).^{27, 30} This result demonstrated that the as-prepared TESPAT has good electroactivity.

3.2 Anticorrosive Electroactive Aniline Tetramer-containing Hybrid Materials through Sol-gel process

3.2.1 Structural and Electrochemical Characterization of Hybrid Materials

A novel electroactive aniline tetramer-containing hybrid material was obtained by the sol-gel reaction of TESPAT with TEMS, as shown in Scheme 3. The molecular structure of the obtained hybrid materials was confirmed by FTIR spectra, as shown in Figure 5. For TEMS, the strong absorption peaks at 1113, 1058, and 958 cm^{-1} are assigned to the asymmetrical stretching vibrations of $\text{Si-OC}_2\text{H}_5$.³¹ As discussed above

(Figure 1b), the sharp peak appears at 1166 cm^{-1} ascribed to stretching vibrations of C-O in Si-OC₂H₅ group of TESPAT. However, these peaks have disappeared and a new absorbance of Si-OH at 915 cm^{-1} appears after sol-gel process (Figure 5b and 5c), indicating that the hydrolysis reaction occurred. Furthermore, the new strong absorbance bands around 1121 and 1031 cm^{-1} demonstrated that the hybrid materials have formed the Si-O-Si network (Figure 5c). In addition, the hybrid materials have good thermal stability due to the formation of the Si-O-Si network (Figure 6). The morphology of the hybrid material coating was displayed in SEM images as shown in Figure 7. The pure silica showed a rough surface with many microcracks, while the hybrid material exhibited a relatively smooth surface, which is possibly due to the incorporation of organic content making the coating more flexible.

The electroactivity of the resulting hybrid materials was investigated by CV, as can be seen in Figure 8. Only one well-defined oxidation/reduction peak at 0.516 V was observed for the hybrid material in HCl aqueous solution, which could be ascribed to the transition from a LEB form to an EB form. This result is in agreement with the electrochemical property of poly(methacrylamide) containing aniline tetramer side chains.³² Therefore, the AT segments in the hybrid materials maintain their electroactivity.

PAN had been previously reported as an advanced anticorrosive coating material due to its redox catalytic properties of conjugated structures that induced the formation of a passive layer of metal oxide, resulting in effective protection against corrosion on various metallic surfaces.^{22, 23, 33, 34} Therefore, it is conceivable that the

redox behavior of the as-prepared hybrid materials would probably display an enhanced anticorrosive performance similar to that of PAN, as discussed in the following sections.

3.2.2 Anticorrosion Behaviors of Hybrid Materials

A series of electrochemical measurements were used to investigate the anticorrosion behaviors of the hybrid materials. Figure 9 shows the Tafel polarization curves of bare, pure silica-coated and hybrid material-coated Q235 steel after immersion in 3.5% NaCl for 24 h. The cathodic and anodic branches of the polarization curves displayed a typical Tafel behavior. Generally, Tafel regions are identified and corrosion parameters are determined by superimposing a straight line along the linear portion of the cathodic and anodic curve and extrapolating it to corrosion potential (E_{corr}). Therefore, the corrosion current density (i_{corr}), corrosion potential (E_{corr}), anodic and cathodic Tafel slopes (b_a , b_c) were determined from the extrapolation of the Tafel Zone of the cathodic and anodic branches and then summarized in Table 1.

The protection efficiency values were calculated using the following equation:²³

$$P_{EF} \% = \frac{i_{corr}(uncoated) - i_{corr}(coated)}{i_{corr}(uncoated)} \times 100\%$$

Tafel plot of the hybrid material-coated Q235 electrode gave a corrosion potential of $E_{corr} = -0.557$ V, which was found to be more positive than pure silica-coated (-0.592 V) and bare Q235 steel (-0.693 V). The shift of the E_{corr} is probably due to the oxide formation induced by the EB-to-LEB transition.³⁵ Furthermore, the i_{corr} value of the

Q235 electrode coated with the hybrid material ($1.32 \mu\text{A cm}^{-2}$) was much lower than that of pure silica-coated ($10.1 \mu\text{A cm}^{-2}$) and bare Q235 steel ($17.1 \mu\text{A cm}^{-2}$), which was only one tenth of the bare Q235 steel. Moreover, the absolute values of b_a and b_c of hybrid material were found to be larger than those of bare Q235 carbon steel, suggesting that both of the cathodic and anodic reaction were inhibited in the Q235 electrode coated with the hybrid material. It was noted that the $P_{\text{EF}}\%$ of the hybrid material (92.3%) was much higher than that of pure silica (38.6%). When the metal is step by step oxidized into metal oxide forming dense oxide barrier for corrosive ions penetration, PAN (or oligoaniline) itself is reduced to lower oxidation state since the electrochemical potential of PAN is much higher than that of Fe.³⁶ Moreover, PAN can be oxidized to its original oxidation state by the oxygen in the air, and a new run of redox reaction can start.³⁶ Therefore, the enhanced anticorrosive performance of the hybrid material coated on Q235 steel may result from the redox catalytic capabilities of the AT units in the hybrid material, then forming passive metal oxide layers on the iron surface.^{19, 37, 38}

EIS was further explored to evaluate the degradation processes of various samples immersed in 3.5% NaCl solution as a function of time, as shown in Figure 10. The impedance modulus at low frequency (such as $|Z|_{0.01\text{Hz}}$) represents the ability of the coating to impede the flow of current between anodic and cathodic areas, which is inversely proportional to corrosion rate.³⁹ The $|Z|_{0.01\text{Hz}}$ value of the hybrid material-coated Q235 electrode was $101.5 \text{ K}\Omega \text{ cm}^2$ after 24 h immersion (Figure 9d), which was much higher than that of pure silica-coated ($1.4 \text{ K}\Omega \text{ cm}^2$) (Figure 9a).

It can be seen that all the EIS exhibited a capacitive arc at the high frequency and a bigger capacitive arc at the middle-low frequency. The diameters of the two capacitive arcs decreased with exposure times, suggesting the gradual failure of the hybrid material coatings. For quantitative estimate the evolution of the anticorrosion properties of the hybrid material, EIS data were fitted with equivalent circuit, as shown in Figure 11 and the fitted parameters were listed in Table 2. In the equivalent circuit, R_s is the solution resistance. As the coating may exhibit heterogeneous nature due to the presence of pores and the failure of coating, the constant phase element Q in the equivalent circuit was used to represent capacitance. Q is expressed as ω^{-n}/Y_0 ($\cos n\pi/2 + j\sin n\pi/2$), where Y_0 and n are the constant and exponent, respectively, ω is the angular frequency.⁴⁰ R_c and Q_c represent the coating resistance and coating capacitance, respectively. R_{ct} and Q_{dl} represent the charge-transfer resistance and double-layer capacitance, respectively. Figure 12 showed the time dependence of R_c and R_{ct} of the hybrid material coatings in 3.5% NaCl solution. R_c represents the physical barrier properties of the coating while the R_{ct} is determined by the faradaic process of charge transfer process.⁴¹ It is rather remarkable that both the R_c and R_{ct} of the hybrid material-coated electrodes were found to be much higher than those of pure silica. The change of Q_{dl} is attributed to change of real area of the corroded electrode during the corrosion process.⁴² And the Q_c values of the hybrid material coatings were ranged from 0.012 to 0.021 $\mu\text{F cm}^{-2} \text{Hz}^{1-n_1}$ (10 wt% TESPAT-TEMS), and 0.0159 to 0.0261 $\mu\text{F cm}^{-2} \text{Hz}^{1-n_1}$ (5 wt% TESPAT-TEMS), respectively, which were much lower than that of pure silica coating during the same exposure times. In a word, both

the polarization curves and EIS results clearly demonstrated that the hybrid materials protect the Q235 steel against corrosion better than the pure silica coating does.

It should be noted that the R_c values of 5 wt% TESPAT-TEMS coating were higher than other coatings during the whole immersion times, suggesting its good film forming property and better barrier property. However, the R_{ct} values of 10 wt% TESPAT-TEMS coating exhibit better protective effect, because more TESPAT improved the passivation performance on metal matrix,³⁵ but excessive TESPAT may affect the film forming property of hybrid coating (its R_c decreased rapidly from 3031 to 660 $\Omega \text{ cm}^2$ with the increase of immersing time). Moreover, the i_{corr} values of 5 wt % TESPAT-TEMS (1.32 $\mu\text{A cm}^{-2}$) was much lower than that of 10 wt % TESPAT-TEMS (3.89 $\mu\text{A cm}^{-2}$), and the E_{corr} of 5 wt % TESPAT-TEMS (-0.557 V) was found to be more positive than that of 10 wt % TESPAT-TEMS (-0.646 V), as shown in Table 1. These results mentioned above indicated that hybrid materials containing 5 wt% TESPAT exhibited better anticorrosion performance based on carbon steel.

4. Conclusions

We have synthesized a novel electroactive silsesquioxane precursor, *N*-(3-triethoxysilylpropylureido) aniline tetramer (TESPAT) via one-step coupling reaction between aniline tetramer and TESPIC. UV-vis spectra and cyclic voltammetry confirmed the unique electroactivity of TESPAT. Furthermore, new electroactive siliceous hybrid materials have also been successfully prepared through the sol-gel reactions of TESPAT with TEMS at various compositions. The hybrid

material exhibits remarkably enhanced corrosion protection as its protection efficiency is better than that of pure silica by a factor of 2.4, based on potentiodynamic polarization measurements performed under saline condition. The significantly improved anticorrosion performance is attributed to the redox catalytic capabilities of the AT units in the hybrid materials.

Acknowledgements

The research is financially supported by the National Natural Science Foundation of China (Grant no. 21404112) and China Postdoctoral Science Foundation (Grant no. 2014M561798). The authors thank Dr. Qing-Yun Wu in Ningbo University for her suggestion and discussion.

References

1. C. Sanchez, B. Lebeau, F. Chaput and J. P. Boilot, *Advanced Materials*, 2003, **15**, 1969-1994.
2. A. Walcarius, *Chem. Mat.*, 2001, **13**, 3351-3372.
3. J. J. E. Moreau and M. Wong Chi Man, *Coordination Chemistry Reviews*, 1998, **178-180**, Part 2, 1073-1084.
4. M. R. Detty, R. Ciriminna, F. V. Bright and M. Pagliaro, *Accounts Chem. Res.*, 2014, **47**, 678-687.
5. D. Wang and G. P. Bierwagen, *Progress in Organic Coatings*, 2009, **64**, 327-338.
6. A. Walcarius, D. Mandler, J. A. Cox, M. Collinson and O. Lev, *Journal of Materials Chemistry*, 2005, **15**, 3663-3689.
7. M. L. Zheludkevich, I. M. Salvado and M. G. S. Ferreira, *Journal of Materials Chemistry*, 2005, **15**, 5099-5111.
8. S. V. Lamaka, M. F. Montemor, A. F. Galio, M. L. Zheludkevich, C. Trindade, L. F. Dick and M. G. S. Ferreira, *Electrochimica Acta*, 2008, **53**, 4773-4783.
9. P. Deshpande, N. Jadhav, V. Gelling and D. Sazou, *J Coat Technol Res*, 2014, **11**, 473-494.
10. H. Bhandari, S. A. Kumar and S. K. Dhawan, *Conducting Polymer Nanocomposites for Anticorrosive and Antistatic Applications*, 2012.
11. S. P. Zhou, H. M. Zhang, Q. Zhao, X. H. Wang, J. Li and F. S. Wang, *Carbon*, 2013, **52**, 440-450.
12. Q. Lu, Q. Zhao, H. M. Zhang, J. Li, X. H. Wang and F. S. Wang, *Acs Macro Letters*, 2013, **2**, 92-95.
13. Y. Kim, K. Teshima and N. Kobayashi, *Electrochimica Acta*, 2000, **45**, 1549-1553.
14. K. Brazdziuvienė, I. Jurevičiūtė and A. Malinauskas, *Electrochimica Acta*, 2007, **53**, 785-791.

15. Y. Chen, X. H. Wang, J. Li, J. L. Lu and F. S. Wang, *Electrochimica Acta*, 2007, **52**, 5392-5399.
16. Y. P. Li, H. M. Zhang, X. H. Wang, J. Li and F. S. Wang, *Corrosion Science*, 2011, **53**, 4044-4049.
17. T. I. Yang, C. W. Peng, Y. L. Lin, C. J. Weng, G. Edgington, A. Mylonakis, T. C. Huang, C. H. Hsu, J. M. Yeh and Y. Wei, *Journal of Materials Chemistry*, 2012, **22**, 15845-15852.
18. F. Chen and P. Liu, *ACS Applied Materials & Interfaces*, 2011, **3**, 2694-2702.
19. K.-Y. Huang, Y.-S. Jhuo, P.-S. Wu, C.-H. Lin, Y.-H. Yu and J.-M. Yeh, *European Polymer Journal*, 2009, **45**, 485-493.
20. H. Y. Huang, T. C. Huang, T. C. Yeh, C. Y. Tsai, C. L. Lai, M. H. Tsai, J. M. Yeh and Y. C. Chou, *Polymer*, 2011, **52**, 2391-2400.
21. S.-C. Lin, C.-S. Wu, J.-M. Yeh and Y.-L. Liu, *Polymer Chemistry*, 2014, **5**, 4235.
22. K. C. Chang, H. I. Lu, C. W. Peng, M. C. Lai, S. C. Hsu, M. H. Hsu, Y. K. Tsai, C. H. Chang, W. I. Hung, Y. Wei and J. M. Yeh, *Acs Applied Materials & Interfaces*, 2013, **5**, 1460-1467.
23. C.-J. Weng, C.-H. Chang, C.-W. Peng, S.-W. Chen, J.-M. Yeh, C.-L. Hsu and Y. Wei, *Chemistry of Materials*, 2011, **23**, 2075-2083.
24. Z. C. Sun, L. Kuang, X. B. Jing, X. H. Wang, J. Li and F. S. Wang, *Chemical Journal of Chinese Universities*, 2002, **23**, 496-499.
25. H. Wang, P. Guo and Y. Han, *Macromolecular Rapid Communications*, 2006, **27**, 63-68.
26. Z. Yang, X. Wang, Y. Yang, Y. Liao, Y. Wei and X. Xie, *Langmuir*, 2010, **26**, 9386-9392.
27. L. Chen, Y. Yu, H. Mao, X. Lu, W. Zhang and Y. Wei, *Materials Letters*, 2005, **59**, 2446-2450.
28. Y. Guo, A. Mylonakis, Z. T. Zhang, P. I. Lelkes, K. Levon, S. X. Li, Q. W. Feng and Y. Wei, *Macromolecules*, 2007, **40**, 2721-2729.
29. H. Cui, Y. Liu, Y. Cheng, Z. Zhang, P. Zhang, X. Chen and Y. Wei, *Biomacromolecules*, 2014, **15**, 1115-1123.
30. Y. Wu, B. Guo and P. X. Ma, *ACS Macro Letters*, 2014, **3**, 1145-1150.
31. F. Rubio, J. Rubio and J. L. Oteo, *Spectroscopy Letters*, 1998, **31**, 199-219.
32. R. Chen and B. C. Benicewicz, *Macromolecules*, 2003, **36**, 6333-6339.
33. D. W. DeBerry, *Journal of The Electrochemical Society*, 1985, **132**, 1022-1026.
34. Y. Wei, C. C. Yang, T. Z. Ding, J. M. Yeh and G. Wei, *Abstracts of Papers of the American Chemical Society*, 1996, **211**, 128-PMSE.
35. H. Y. Huang, T. C. Huang, J. C. Lin, J. H. Chang, Y. T. Lee and J. M. Yeh, *Materials Chemistry and Physics*, 2013, **137**, 772-780.
36. J. L. Lu, N. J. Liu, X. H. Wang, J. Li, X. B. Jing and F. S. Wang, *Synthetic Metals*, 2003, **135**, 237-238.
37. T. C. Huang, Y. A. Su, T. C. Yeh, H. Y. Huang, C. P. Wu, K. Y. Huang, Y. C. Chou, J. M. Yeh and Y. Wei, *Electrochimica Acta*, 2011, **56**, 6142-6149.
38. K.-Y. Huang, C.-L. Shiu, P.-S. Wu, Y. Wei, J.-M. Yeh and W.-T. Li, *Electrochimica Acta*, 2009, **54**, 5400-5407.
39. T. T. X. Hang, T. A. Truc, N. T. Duong, N. Pébère and M.-G. Olivier, *Prog. Org. Coat.*, 2012, **74**, 343-348.
40. S. Liu, H. Sun, L. Sun and H. Fan, *Corrosion Sci.*, 2012, **65**, 520-527.
41. H. Huang, X. Guo, G. Zhang and Z. Dong, *Corrosion Sci.*, 2011, **53**, 1700-1707.
42. H. Huang, X. Guo, G. Zhang and Z. Dong, *Corrosion Sci.*, 2011, **53**, 3446-3449.

Figure legends

Scheme 1. Synthesis of *N*-(3-triethoxysilylpropylureido) aniline tetramer (TESPAT).

Scheme 2. Molecular structure of TESPAT in various oxidation states.

Scheme 3. Preparation of aniline tetramer-containing hybrid materials through sol-gel process.

Figure 1. FTIR spectra of AT (a) and TESPAT (b).

Figure 2. ^1H NMR spectra of AT (a) and TESPAT (b).

Figure 3. UV-vis spectra of AT (a) and TESPAT (b). Solvent: ethanol.

Figure 4. Cyclic voltammogram of TESPAT in 1 M HCl solution.

Figure 5. FTIR spectra of TEMS (a), TESPAT (b) and 10 wt% TEMS-TESPAT (c).

Figure 6. TGA of hybrid materials from TESPAT-TEMS at different percentage of TESPAT.

Figure 7. SEM images of pure silica (A) and hybrid material from TESPAT-TEMS at 5 wt% TESPAT (B).

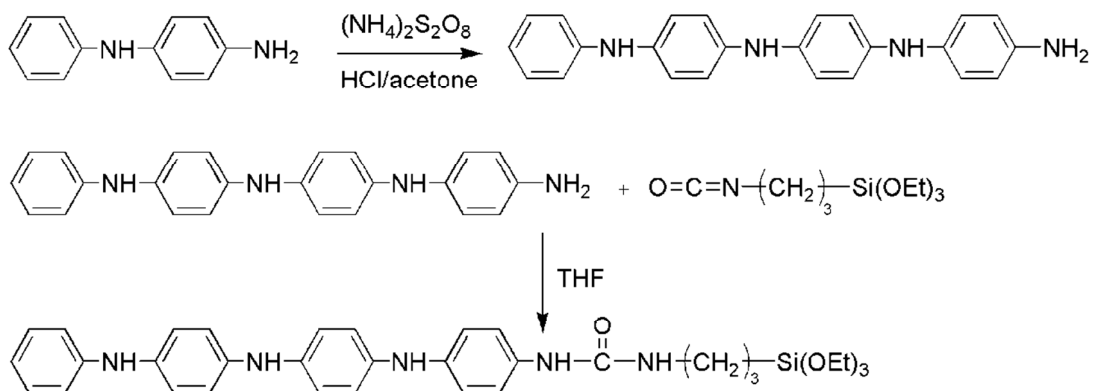
Figure 8. Cyclic voltammogram of hybrid materials from TESPAT-TEMS with 10 wt% TESPAT in 1 M HCl solution.

Figure 9. The polarization curves of bare (a), pure silica-coated (b) and hybrid material-coated (c) Q235 steel electrodes after immersion in 3.5% NaCl for 24 h.

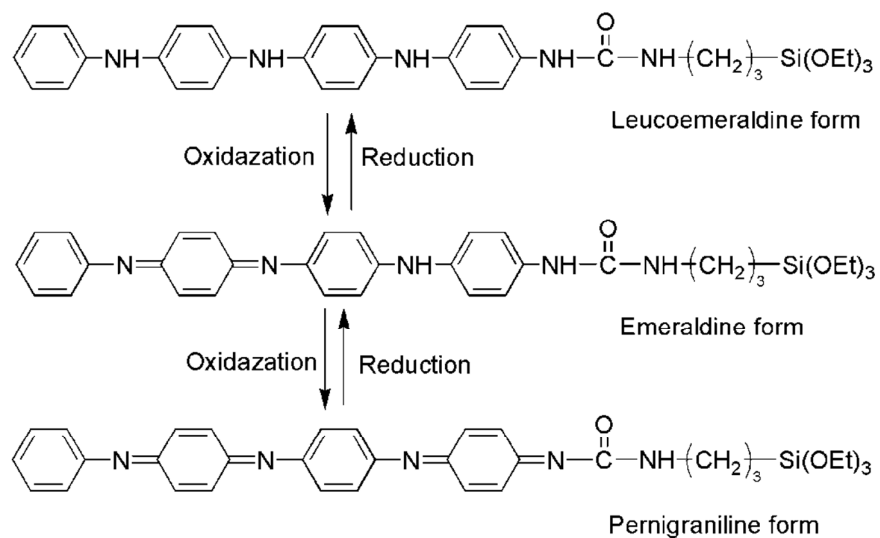
Figure 10. The Nyquist and Bode plots of pure silica from TEMS (a) and the hybrid materials from TESPAT-TEMS at different percentage of TESPAT: (b) 2 wt%; (c) 5 wt% ; (d) 10 wt% immersed in 3.5% NaCl solution as a function of time.

Figure 11. The equivalent circuit used to fit the EIS data.

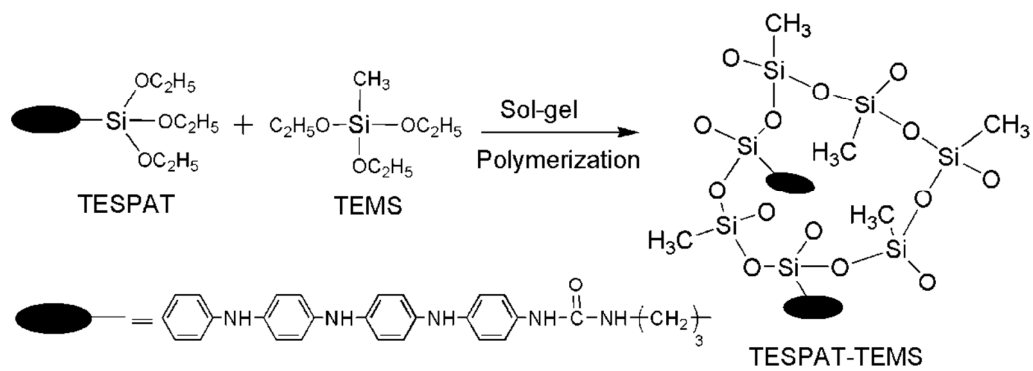
Figure 12. Time dependence of the coating resistance (a) and charge transfer resistance (b) of the hybrid materials from TESPAT-TEMS at different percentage of TESPAT (0-5 wt %) coated Q235 electrodes exposed to 3.5% NaCl solution.



Scheme 1. Synthesis of *N*-(3-triethoxysilylpropylureido) aniline tetramer (TESPAT).



Scheme 2. Molecular structure of TESPAT in various oxidation states.



Scheme 3. Preparation of aniline tetramer-containing hybrid materials through sol-gel process.

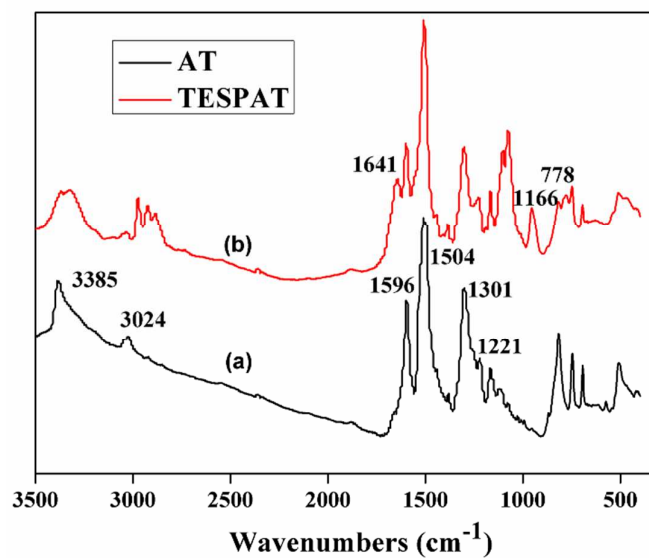


Figure 1. FTIR spectra of AT (a) and TESPAT (b).

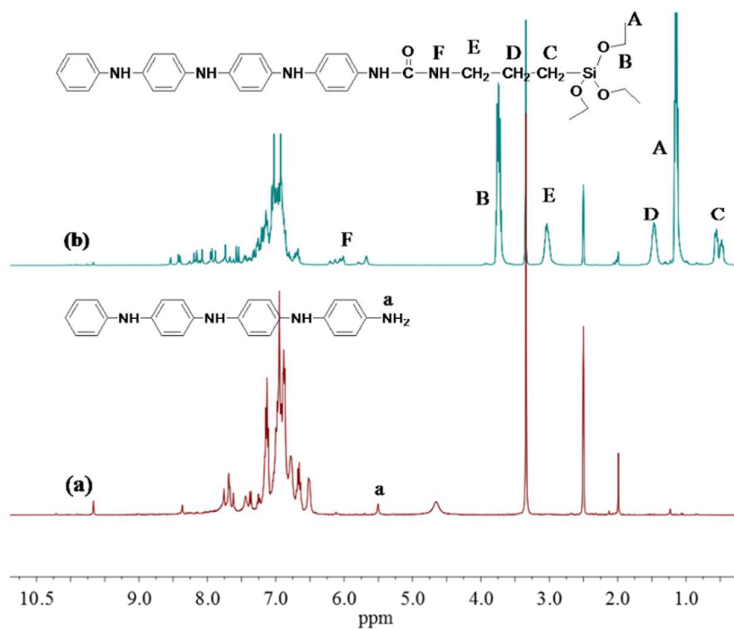


Figure 2. ^1H NMR spectra of AT (a) and TESPAT (b).

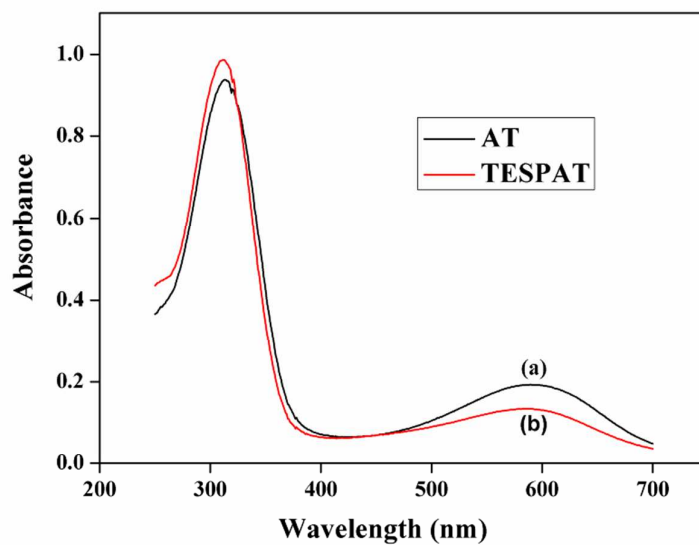


Figure 3. UV-vis spectra of AT (a) and TESPAT (b). Solvent: ethanol.

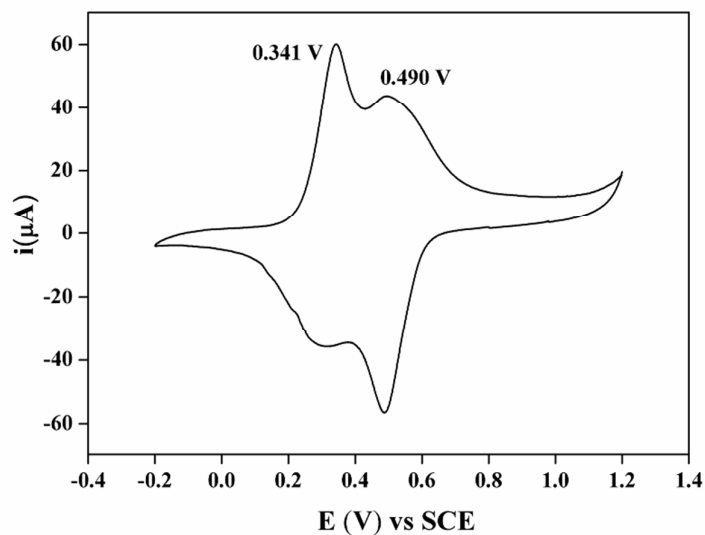


Figure 4. Cyclic voltammogram of TESPAT in 1 M HCl solution.

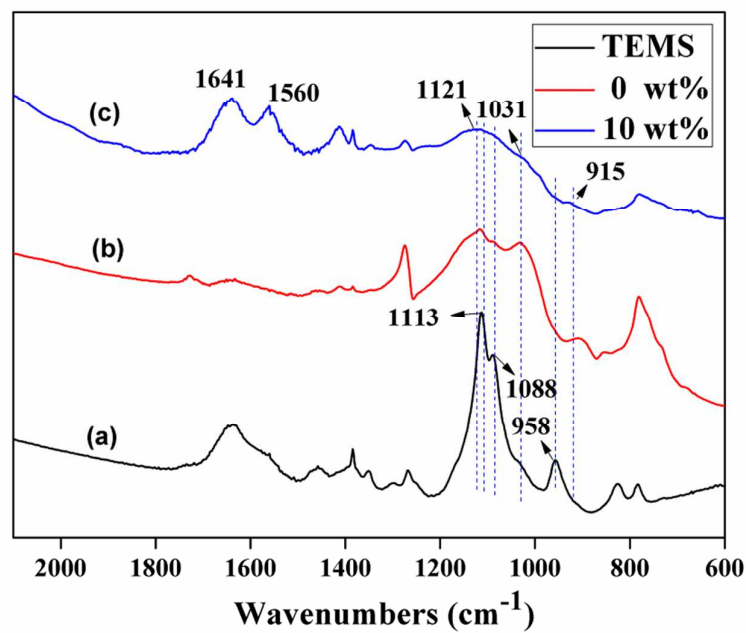


Figure 5. FTIR spectra of TEMS (a), TESPAT (b) and 10 wt% TEMS-TESPAT (c).

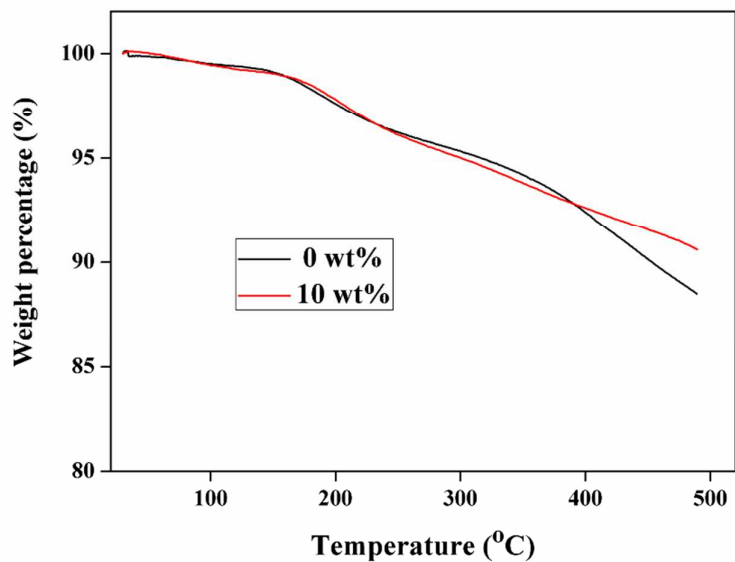


Figure 6. TGA of hybrid materials from TESPAT-TEMS at different percentage of TESPAT.

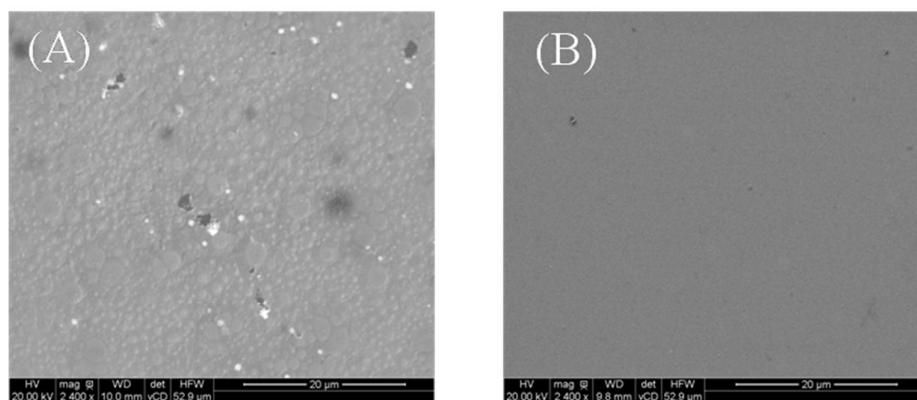


Figure 7. SEM images of pure silica (A) and hybrid material from TESPAT-TEMS at 5 wt% TESPAT (B).

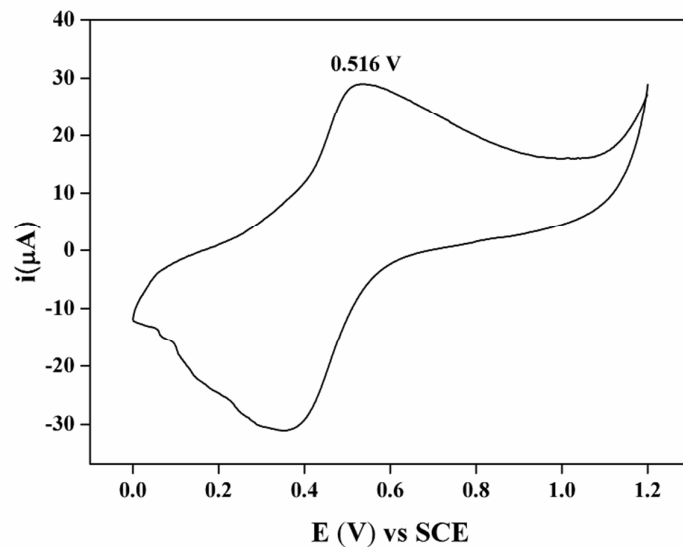


Figure 8. Cyclic voltammogram of hybrid materials from TESPAT-TEMS with 10 wt% TESPAT in 1 M HCl solution.

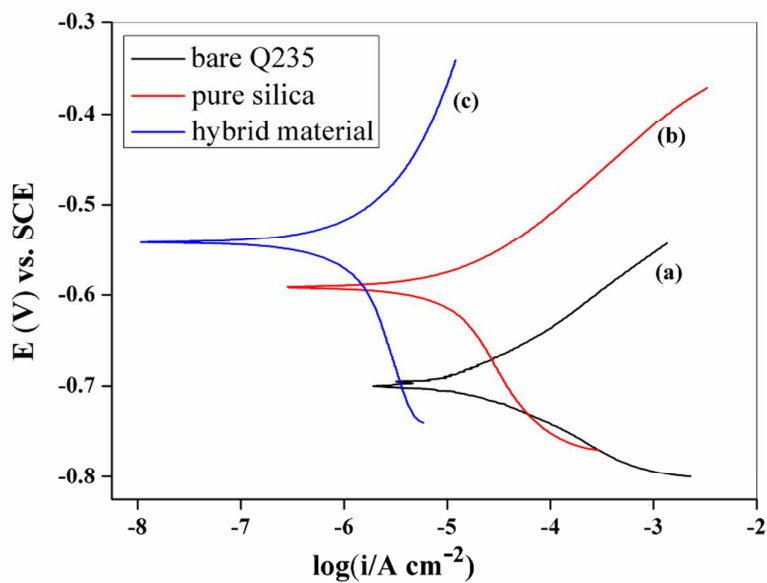


Figure 9. The polarization curves of bare (a), pure silica-coated (b) and hybrid

material (5 wt% TESPAT)-coated (c) Q235 steel electrodes after immersion in 3.5% NaCl for 24 h.

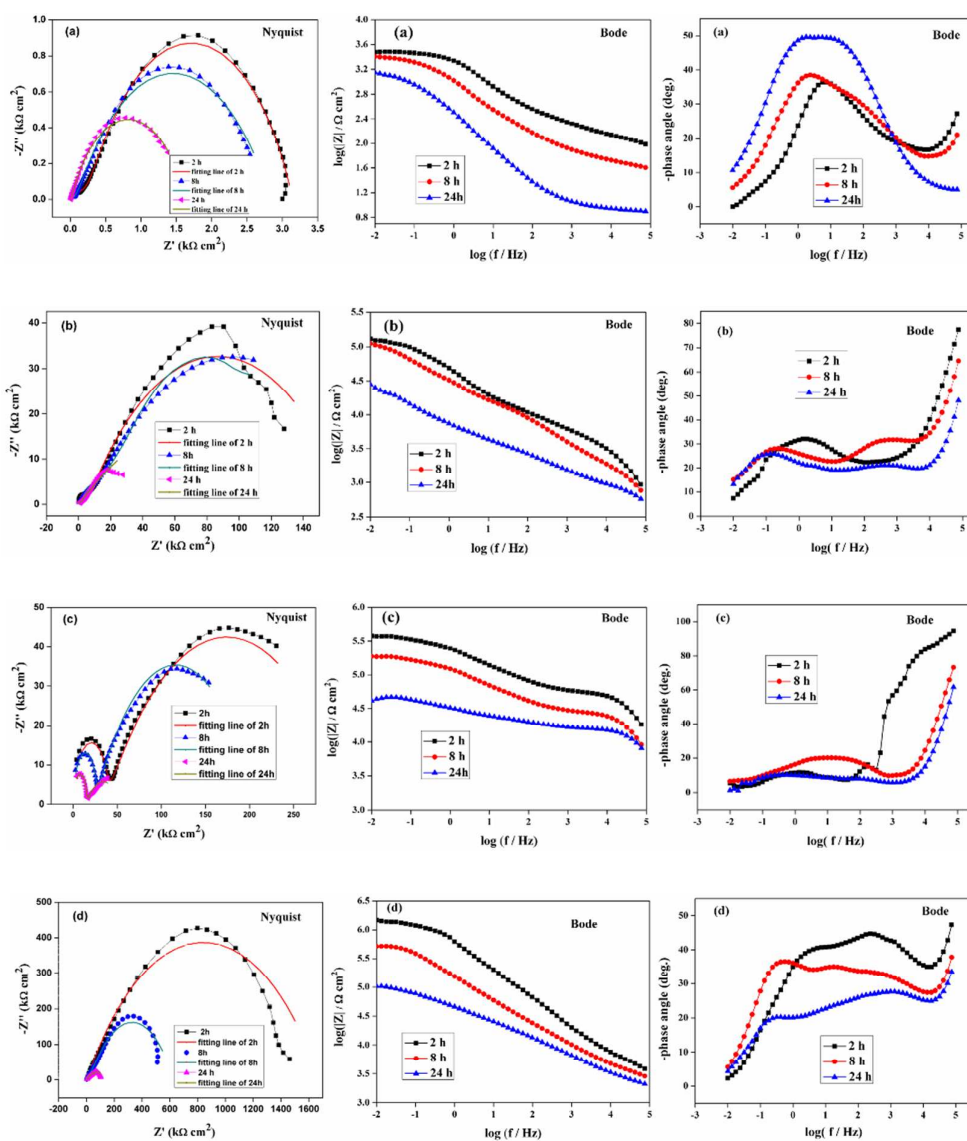


Figure 10. The Nyquist and Bode plots of pure silica from TEMS (a) and the hybrid materials from TESPAT-TEMS at different percentage of TESPAT: (b) 2 wt%; (c) 5 wt%; (d) 10 wt% immersed in 3.5% NaCl solution as a function of time.

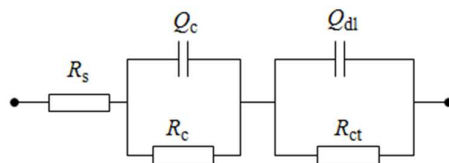


Figure 11. The equivalent circuit used to fit the EIS data.

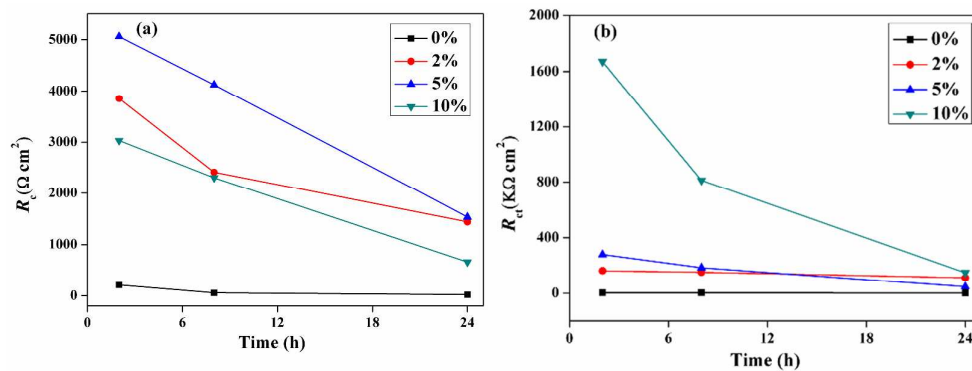


Figure 12. Time dependence of the coating resistance (a) and charge transfer resistance (b) of the hybrid materials from TESPAT-TEMS at different percentage of TESPAT (0-10 wt %) coated Q235 electrodes exposed to 3.5% NaCl solution.

Table 1. Corrosion parameters of bare, pure silica-coated and hybrid material-coated Q235 steel electrodes after immersion in 3.5% NaCl for 24 h.

	E_{corr}	i_{corr}	b_a	b_c	R_p	Thickness	P_{EF}
	V, vs.SCE	$\mu\text{A cm}^{-2}$	mV dec^{-1}	mV dec^{-1}	$\text{K}\Omega \text{cm}^2$	μm	(%)
Bare ^a	-0.693	17.1	72.8	60.2	0.83	-	-
Pure silica ^b	-0.592	10.5	85.9	214.2	2.53	2	38.6
Hybrid material ^c	-0.557	1.32	212.8	333.4	42.73	2	92.3
Hybrid material ^d	-0.646	3.89	94.5	234.6	7.84	2	77.2

^aBare Q235 steel; ^bPure silica from TEMS; ^cHybrid material from TESPAT-TEMS at 5 wt% TESPAT; ^dHybrid material from TESPAT-TEMS at 10 wt% TESPAT.

Table 2. Fitting parameters for the electrical equivalent circuit in Figure 11.

TESPAT content	Time h	R_s Ωcm^2	Q_c $\mu\text{F cm}^{-2} \text{Hz}^{1-n_1}$	n_1	R_c Ωcm^2	Q_{dl} $\mu\text{F cm}^{-2} \text{Hz}^{1-n_2}$	n_2	R_{ct} $\text{K}\Omega \text{cm}^2$
0%	2	0.01	21.9	0.48	210.9	67.7	0.65	3.06
	8	0.01	34.2	0.52	55.1	251	0.55	2.91
	24	0.01	139	0.65	20.1	756	0.63	1.63
2%	2	0.01	0.028	0.83	3856	7.37	0.48	163
	8	0.01	0.435	0.45	2410	15.7	0.46	152
	24	0.01	0.783	1.00	1440	75.6	0.28	36.2
5%	2	0.01	0.0159	0.99	5059	1.56	0.49	279
	8	0.01	0.0258	1.00	4126	2.36	0.47	184
	24	0.01	0.0261	1.00	1532	18.3	0.34	46.6
10%	2h	0.01	0.0122	0.96	3031	0.438	0.55	1671
	8h	0.01	0.0347	0.56	2301	1.92	0.57	812
	24h	0.01	0.0218	1.00	660	8.35	0.54	149